Discretized Gaussian Representation for Tomographic Reconstruction

Shaokai Wu[1], Yuxiang Lu[1], Wei Ji[2], Suizhi Huang[1], Fengyu Yang[3],
Shalayiding Sirejiding[1], Qichen He[1], Jing Tong[1], Yanbiao Ji[1], Yue Ding[1], Hongtao Lu[1]
[1]Shanghai Jiao Tong University, [2]National University of Singapore, [3]Yale University

Abstract

Computed Tomography (CT) is a widely used imaging technique that provides detailed cross-sectional views of objects. Over the past decade, Deep Learning-based Reconstruction (DLR) methods have led efforts to enhance image quality and reduce noise, yet they often require large amounts of data and are computationally intensive. Inspired by recent advancements in scene reconstruction, some approaches have adapted NeRF and 3D Gaussian Splatting (3DGS) techniques for CT reconstruction. However, these methods are not ideal for direct 3D volume reconstruction. In this paper, we reconsider the representation of CT reconstruction and propose a novel Discretized Gaussian Representation (DGR) specifically designed for CT. Unlike the popular 3D Gaussian Splatting, our representation directly reconstructs the 3D volume using a set of discretized Gaussian functions in an end-to-end manner. Additionally, we introduce a Fast Volume Reconstruction technique that efficiently aggregates the contributions of these Gaussians into a discretized volume. Extensive experiments on both real-world and synthetic datasets demonstrate the effectiveness of our method in improving reconstruction quality and computational efficiency. Our code has been provided for review purposes and will be made publicly available upon acceptance.

1. Introduction

When a patient undergoes a Computed Tomography (CT) scan at a hospital, the initial output is not the familiar image seen on the screen, but rather a series of projection data generated by X-ray detectors [19]. This data is then processed by a CT reconstruction algorithm to transform the raw information into a 3D volume, which radiologists examine to assess the patient's condition. This task is challenging due to three main factors. Firstly, the radioactive exposure from a complete CT scan poses significant health risks to patients, limiting the number of projections that can be acquired [35]. Secondly, time constraints in emergency situations require fast reconstruction to enable timely diagnosis [4]. Lastly,
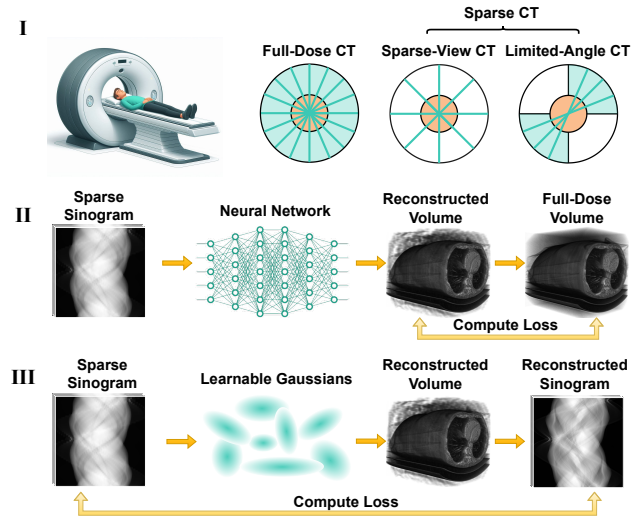

Figure 1. I, Illustration of CT scanning process and two common paradigms of sparse CT: Sparse-View CT and Limited-Angle CT. II, deep-learning reconstruction (DLR) methods, which learn to reconstruct the volume under the supervision of projection-image pairs. III, Our proposed Discretized Gaussian Representation (DGR), directly optimizing a set of learnable Gaussians under the supervision of projection domain.

the method must be generalizable across various CT configurations, such as different numbers of views and angles, to accommodate diverse imaging protocols and patient conditions [29].

Hitherto, Deep Learning-based Reconstruction (DLR) methods have been extensively studied in CT reconstruction. These methods have evolved from traditional convolutional neural networks (CNNs) such as FBPConvNet [16] and REDCNN [5], which focus on denoising reconstructed images, to dual-domain approaches like HDNet [15], which optimize in both the projection and image domains. More recently, diffusion-based methods, including DiffusionMBIR [7] and SWORD [31], leverage score functions as priors to guide the reconstruction process. Despite the advancements of these methods, they still fail to address the latter two challenges outlined above. Neural network-based approaches are often computationally intensive due to the

training process and are not easily adaptable to different CT configurations. For instance, a model trained on cone-beam CT data may not perform well on fan-beam CT data, a network trained on chest scans may be less effective for head scans, and a model trained on healthy patients may struggle with scans of patients with diseases.

These challenges have driven the development of instance-level reconstruction methods, which aim to provide tailored reconstructions for each patient. The success of NeRF [25] and 3D Gaussian Splatting (3DGS) [18] in scene reconstruction has inspired the adaptation of these techniques for CT reconstruction. However, NeRF-based methods typically require hours to reconstruct a single volume, which is impractical for an efficient clinical workflow. In contrast, 3DGS-based methods do not directly reconstruct a 3D volume but rather render the scene dynamically. As noted by Zha et al. [35], 3DGS-based methods are not well-suited for direct 3D volume reconstruction, prompting their proposal of a density voxelization technique to address this limitation.

In this paper, we ask: Do we really need to rely on neural networks or adapt scene reconstruction methods for CT reconstruction? Is it possible to design a method that can directly learn to reconstruct a 3D volume from projection data in an end-to-end manner? Driven by these questions, we fundamentally reconsider the representation: since the target volume is discretized and aligned to a 3D grid, why not directly represent the volume as a set of discretized Gaussian functions? This insight guided our approach, yet we encountered a challenge: setting discretized Gaussians in a 3D grid renders the process non-differentiable. To resolve this, we address the discrepancy between continuous and discretized spaces by aligning the Gaussians from continuous space to the discretized grid while preserving each Gaussian's contribution to its local region.

Another challenge arises in computing each Gaussian's contribution to the volume, a highly complex and time-consuming task. We tackle this by restricting each Gaussian's contribution to a localized region around each voxel and decomposing the high-dimensional matrix multiplication into a series of lower-dimensional multiplications, reducing the original reconstruction time by 90%. Our DGR method (Figure 1) is highly efficient, reconstructing a 3D volume with dimensions $256 \times 256 \times 256$ from over 150K Gaussians within 0.09 seconds (Table 8). The entire training process achieves plausible results in under 5 minutes, with convergence reached in approximately 15 minutes. We also demonstrate that our method significantly improves reconstruction quality on both real-world and synthetic datasets, outperforming both DLR and reconstruction-based methods without additional modifications. Notably, our method is not an adaptation of 3DGS for CT reconstruction but introduces a novel Discretized Gaussian Representation.

We summarize our main contributions as follows:

- We propose a Discretized Gaussian Representation (DGR) for CT reconstruction that directly learns to reconstruct the 3D volume from a set of discretized Gaussians in an end-to-end manner.
- We introduce a fast volume reconstruction technique that efficiently aggregates the contributions of the Gaussians into a discretized volume in a highly parallelized way, significantly reducing reconstruction time.
- We conduct extensive experiments in both real-world and synthetic datasets against both DLR methods and reconstruction-based approaches, demonstrating both effectiveness and efficiency.

2. Background

2.1. Deep Learning Reconstruction (DLR)

Deep Learning Reconstruction (DLR) methods have always been heated in the field of CT reconstruction since the success of deep neural networks in image processing [27]. Traditional DLR approaches can be grouped into two main categories: direct and indirect learning. Direct learning methods train networks to reconstruct images directly from projection data (sinograms). Examples include AUTOMAP [36], which employs manifold approximation, and iRadonMAP [13], which uses learnable filtering and back-projection. In contrast, indirect learning methods [5, 12, 16, 17] approach CT reconstruction as a high-level denoising task. These methods process raw projection data through FBP or IR into the image domain and train networks to map noisy images to clean images. Some indirect methods leverage dual-domain knowledge (projection and image domains) to guide the reconstruction, such as in HDNet [15].

Recent advancements in DLR have led to the development of diffusion models that further guide the reconstruction process. Models like MCG [6], DiffusionMBIR [7], and SWORD [31] learn the score function as a prior, helping manage noise and artifacts in the reconstructed images. However, diffusion-based methods are computationally more intensive than traditional DLR, limiting their practicality in clinical settings. Still, DLR methods can improve generalization and performance by training on large datasets with diverse imaging conditions, ultimately achieving higher reconstruction quality.

2.2. Reconstruction-Based Methods

Reconstruction-based methods form another category of CT reconstruction techniques, focusing on optimizing the reconstruction process by solving an optimization problem. The foundation of these methods lies in iterative reconstruction (IR) [10], where an objective function balances data fidelity with regularization terms to impose prior knowl-
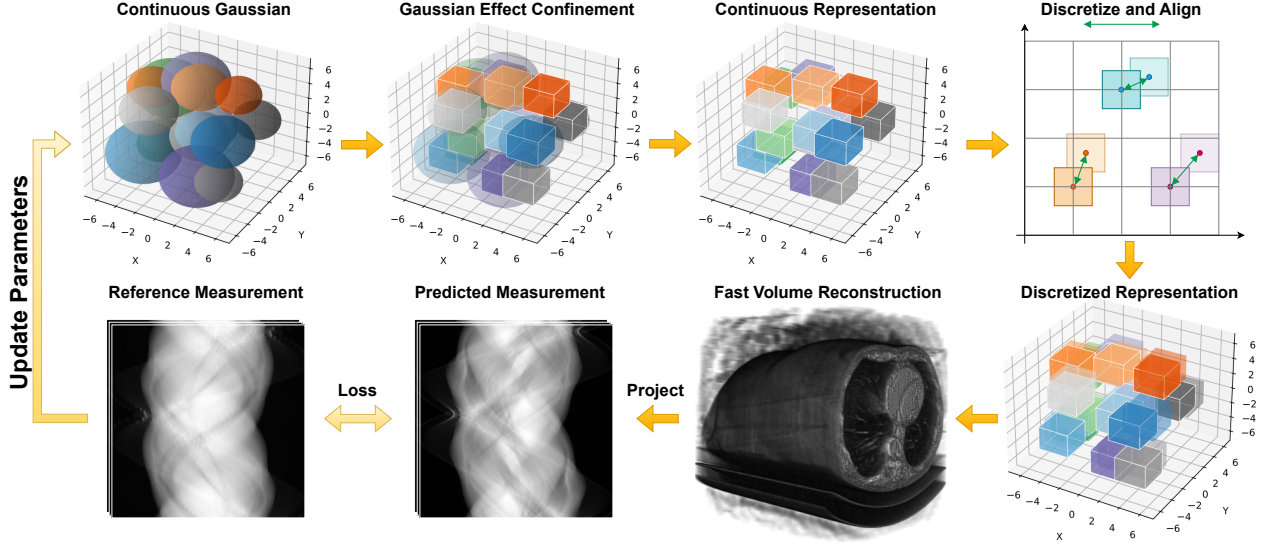
Figure 2. Training pipeline of DGR. This figure illustrates one iteration of the training process. The 3D volume is initially represented by a set of continuous Gaussians, with each Gaussian's contribution limited to a localized region around each voxel. The Gaussians are then discretized onto the 3D grid, where their contributions are aligned to directly reconstruct the entire volume. Using our Fast Volume Reconstruction technique, these contributions are computed in a highly parallelized manner. The entire process is differentiable and end-to-end trainable.

edge or constraints, such as sparsity, smoothness, or edge preservation. Common approaches like algebraic reconstruction techniques (ART), simultaneous iterative reconstruction technique (SIRT), and total variation (TV) regularization are widely adopted to enhance image quality and reduce artifacts compared to direct analytical methods like filtered back projection (FBP) [2].

In recent years, scene reconstruction techniques, such as Neural Radiance Fields (NeRF) [25] and 3D Gaussian Splatting (3DGS) [18], have been adapted for CT reconstruction. NeRF-based approaches like NAF [34] represent the CT scene through a neural network and optimize by minimizing the difference between synthetic and ground-truth projections. Similarly, Intra-Tomo [33] employs a neural network representation and incorporates both local and non-local geometrical priors for optimization. SAX-NeRF [3] enhances accuracy in sparse-view X-ray reconstruction through structure-aware modeling with a transformer backbone and novel ray sampling strategy.

The widely used 3D Gaussian Splatting (3DGS) [18] represents the 3D scene with a set of Gaussians, each depicting a local region of the scene. This approach has inspired several CT reconstruction methods, such as 3DGR-CAR [9], DIF-Gaussian [22], and X-Gaussian [4]. 3DGR-CAR [9] leverages U-Net [27] to initialize Gaussian centers before employing 3DGS for final reconstruction. DIF-Gaussian [22] uses 3D Gaussians to model feature distributions to estimate attenuation coefficients. X-Gaussian adapts 3DGS for novel view synthesis in X-ray imaging.

However, these 3DGS-based methods are not ideal for direct 3D volume reconstruction. Zha et al. [35] have identified integration bias in the standard 3DGS formulation and proposed a density voxelization technique to mitigate this limitation.

3. Preliminary

Problem Formulation Clinical CT imaging involves capturing X-ray projections of the patient from various angles, which are then processed to reconstruct a 3D volume that represents the internal structures. The CT imaging system for a 2D image slice can be described as:

$$y = Ax + \beta, \tag{1}$$

where $x \in \mathbb{R}^{w \times h}$ denotes the 2D image with width w and height h, and $y \in \mathbb{R}^{m \times n}$ represents the projection matrix, with m as the number of projection views and n as the number of detector elements per view. The matrix $A \in \mathbb{R}^{m \times n \times w \times h}$ is the Radon Transform matrix, which maps the geometric relationship between the object and the X-ray source/detector system. This matrix describes how attenuation along various paths within the object contributes to the intensity measured at each detector element across projection views. The noise term $\beta \in \mathbb{R}^{m \times n}$ represents measurement noise.

Optimization Problem. The goal of CT reconstruction is to accurately estimate x from the measurements y. In theory, the Inverse Radon Transform can map measurements

back to the original image; however, practical issues, such as noise in the data and the underdetermined nature of the problem, make perfect reconstruction challenging.

The reconstruction process is commonly formulated as an optimization problem:

$$x^* = \arg\min_x \mathcal{E}(Ax, y) + R(x), \qquad (2)$$

where $\mathcal{E}$ is the data fidelity term, which measures the discrepancy between the estimated measurement Ax and the actual measurement y, often using the L1 or L2 norm. The regularization term $R(x)$ enforces properties like smoothness or sparsity in the reconstructed image, with Total Variation (TV) regularization being a popular choice [24].

4. Methodology

We illustrate our DGR framework in Figure 2. Although DGR is based on Gaussian representation, it is fundamentally different from 3DGS-based methods, and it does not involve any rendering process. DGR aims at directly reconstructing the 3D Tomography volume in an end-to-end and efficient manner. We organize our method section into three parts: Discretized Gaussian Representation (Section 4.1), Fast Volume Reconstruction (Section 4.2), and Optimization (Section 4.2).

4.1. Discretized Gaussian Representation

Continuous Gaussian Representation We begin by introducing the basic formulation of the continuous Gaussian representation for tomography volume reconstruction. We define the Gaussian function centered at μ with covariance Σ as:

$$G(p, \mu, \Sigma) = e^{-\frac{1}{2}(p-\mu)^\top \Sigma^{-1}(p-\mu)}, \qquad (3)$$

where $p \in \mathbb{R}^d, d = 3$ is the 3D point in the scene. The Gaussian function is bell-shaped and symmetric around the mean μ, with the spread controlled by the standard deviation σ that dictates its spread in 3D space. For CT reconstruction, we use a set of learnable *isotropic* Gaussians to represent the entire 3D volume.

Denote the target volume as $V \in \mathbb{R}^{w \times h \times c}$, where w, h, and c are the width, height, and depth of the volume, respectively. The voxel $V(p)$ at point p in the volume is represented as a combination of all the contributions of the n Gaussians in this point:

$$V(p) = \sum_{i=1}^n G(p, \mu_i, \Sigma_i) \cdot I_i, \qquad (4)$$

where $I_i \in \mathcal{R}^+$ is the intensity of the i-th Gaussian, which serves both as the voxel intensity and the weight of the corresponding Gaussian. Note that the volume V is grayscale, and the intensity of each gaussian I_i is a scalar value. In the expression above, $(p-\mu)^\top \Sigma^{-1}(p-\mu)$ is known as the squared Mahalanobis distance, which measures how far the point p is from the center of the Gaussian μ, adjusted for the shape of the distribution. For convenience, we will refer to this quantity as D^2 in the following sections.

However, directly computing the contribution of each Gaussian to the volume will result in unacceptable computational expense (see Table 8). We add an analysis of the computational complexity in Appendix E for interested readers. To address this issue, we restrict the contribution of each Gaussian to a local region around each voxel, which is explained in the next subsection.

Gaussian Effect Confinement Based on the principle that the influence of a Gaussian on a voxel diminishes with increasing distance from the center of the Gaussian, considering only the contributions of Gaussians within a specified proximity of each voxel can accelerate the reconstruction process. While it might seem that restricting the contribution to nearby Gaussians could lead to a loss of distant information, it is important to note that the Gaussians are learnable, and they can adaptively adjust the intensity of each Gaussian to compensate for any missing information from distant Gaussians.

To formalize this concept, we define the local region around each voxel as a rectangular box $B \in \mathbb{R}^{w_0 \times h_0 \times c_0}$ centered on the voxel, where w_0, h_0, and c_0 denote the size of the box, and these dimensions are restricted to odd numbers to ensure that the box is centered around the voxel.

The x-coordinate range within the box spans $[-\frac{w_0-1}{2}, \frac{w_0-1}{2}]$, with similar ranges for $y-$ and $z-$ cooridnates. We can now compute the squared Mahalanobis distance D^2 between the voxel and the Gaussian's mean as:

$$D^2 = B'^T C^{-1} B'. \qquad (5)$$

where C^{-1} is the inverse covariance matrix that adjusts the spread of the Gaussian. The contribution of the $i-th$ Gaussian, centered at μ_i, to the voxel intensity is given by:

$$e^{-\frac{1}{2}D^2} \cdot I_i. \qquad (6)$$

where I_i is the intensity of the $i-th$ Gaussian, as defined previously.

Interestingly, within the local region B, the contribution from the Gaussian is independent of the specific position of its center μ. This can be understood by noting that the coordinates within B are centered around μ, meaning that when we subtract μ from B, we obtain B', which is independent of μ. Mathematically, this implies that the shape of the Gaussian function remains invariant under translation. Shifting μ changes the location of the peak of the Gaussian but does not affect the overall shape of the function.

Discretize and Align In the process of reconstructing a 3D volume V, directly using the continuous mean μ for indexing and summing all Gaussian contributions introduces

4

a challenge: the gradient of μ would not be able to pass through the sum operation. This issue arises because the discretized 3D volume V consists of integer coordinates, while μ is continuous. If we were to simply discretize μ by rounding it to the nearest integer for indexing purposes, the reconstruction process would become non-differentiable, which would hinder optimization.

To address this challenge, instead of directly discretizing μ, we compute each Gaussian's contribution at the discretized grid positions corresponding to the nearest integer coordinates. Specifically, we choose the nearest integer to the center of the box as the index, and we denote this new box centered at the integer as B''.

For clarity, we define the difference between the continuous center μ and its discretized integer counterpart as:

$$\Delta\mu = \mu - \lfloor \mu \rfloor, \tag{7}$$

where $\lfloor \mu \rfloor$ denotes the floor function, which rounds μ to the nearest integer. This $\delta\mu$ represents the offset between the continuous and discretized positions, and it helps ensure the alignment between the continuous Gaussian center and the discretized grid.

We then relate the coordinates of the new box B'' to the original box B by adjusting for this offset. The relation between B'' and B is given by:

$$B''_{n,w_0,h_0,c_0,d} = B'_{w_0,h_0,c_0,d} - \Delta\mu_{n,1,1,1,d,}, \tag{8}$$

where $\Delta\mu_{n,1,1,1,d}$ represents the expansion of $\Delta\mu_{n,d}$ to match the dimensions of B' for element-wise subtraction. This adjustment ensures that each Gaussian is evaluated at the correct location on the discretized grid. This discretization and alignment process allows for smooth optimization, ensuring that gradients can pass through the sum of Gaussian contributions, maintaining the differentiability of the reconstruction process.

4.2. Fast Volume Reconstruction

Parallel Computation The key to the fast reconstruction process lies in efficiently computing the squared Mahalanobis distance D^2 within the local region, as defined in Equation 4. For each voxel, we compute D^2 using the discretized box B'', which leads to:

$$D^2 = B''^T C^{-1} B''. \tag{9}$$

To efficiently handle this computation, we utilize the Einstein summation convention, which allows us to express the sum over indices implicitly. The expression for D^2 is thus:

$$D^2_{n,w_0,h_0,c_0} = \sum_d B''_{n,w_0,h_0,c_0,d} \, C^{-1}_{n,d,d} \, B''_{n,w_0,h_0,c_0,d}.$$

Once the squared Mahalanobis distance D^2 is computed, the contributions of all Gaussians are summed to form the final reconstructed volume, as detailed in the following content.

Decomposition To further reduce computation, we decompose the large Einstein summation into smaller, more manageable sums. The squared Mahalanobis distance D^2 can be decomposed into a combination of the following four smaller Einstein sums:

$$B'^T C^{-1} B'_{n,w_0,h_0,c_0} = \sum_d B'_{w_0,h_0,c_0,d} \, C^{-1}_{n,d,d} \, B'_{w_0,h_0,c_0,d},$$

$$B'^T C^{-1} \Delta\mu_{n,w_0,h_0,c_0} = \sum_d B'_{w_0,h_0,c_0,d} \, C^{-1}_{n,d,d} \, \Delta\mu_{n,1,1,d},$$

$$\Delta\mu^T C^{-1} B'_{n,w_0,h_0,c_0} = \sum_d \Delta\mu_{n,1,1,d} \, C^{-1}_{n,d,d} \, B'_{w_0,h_0,c_0,d},$$

$$\Delta\mu^T C^{-1} \Delta\mu_{n,1,1,1} = \sum_d \Delta\mu_{n,1,1,d} \, C^{-1}_{n,d,d} \, \Delta\mu_{n,1,1,d},$$

Subsequently, we can compute the squared Mahalanobis distance D^2 as:

$$\begin{aligned} D^2_{n,w_0,h_0,c_0} = {} & B'^T C^{-1} B'_{n,w_0,h_0,c_0} - B'^T C^{-1} \Delta\mu_{n,w_0,h_0,c_0} \\ & - \Delta\mu^T C^{-1} B'_{n,w_0,h_0,c_0} + \Delta\mu^T C^{-1} \Delta\mu_{n,1,1,1}. \end{aligned}$$

The final contribution of the Gaussians within the local region is computed as:

$$\Gamma = e^{-\frac{1}{2} D^2_{n,w_0,h_0,c_0}} \cdot I, \tag{10}$$

where $\Gamma \in \mathbb{R}^{n \times w_0 \times h_0 \times c_0}$ represents the contributions of the n Gaussians within the local region. This expression allows us to calculate the contributions in a highly efficient manner, which reduces time complexity without compromising space complexity. Specifically, $B'_{w_0,h_0,c_0,d}$ is only $\frac{1}{n}$ the size of $B''_{n,w_0,h_0,c_0,d}$, enabling far more efficient computations. Table 8 provides quantitative evidence of this efficiency boost.

It is important to note that Γ is not the final volume V, but the contribution of each Gaussian within the local region. The next step we need to add the contribution of each Gaussian to its corresponding voxels in the volume. For each contribution $\Gamma_{i,x,y,z}$ of the i-th Gaussian to the voxel at position (x, y, z) in the volume, we have:

$$V_{x,y,z} \leftarrow V_{x,y,z} + \Gamma_{i,x,y,z}. \tag{11}$$

This step is performed for all Gaussians, ensuring that the contributions are accumulated in the correct positions within the volume. We also include a highly parallelized implementation of this update process in our codebase to further accelerate the reconstruction process.

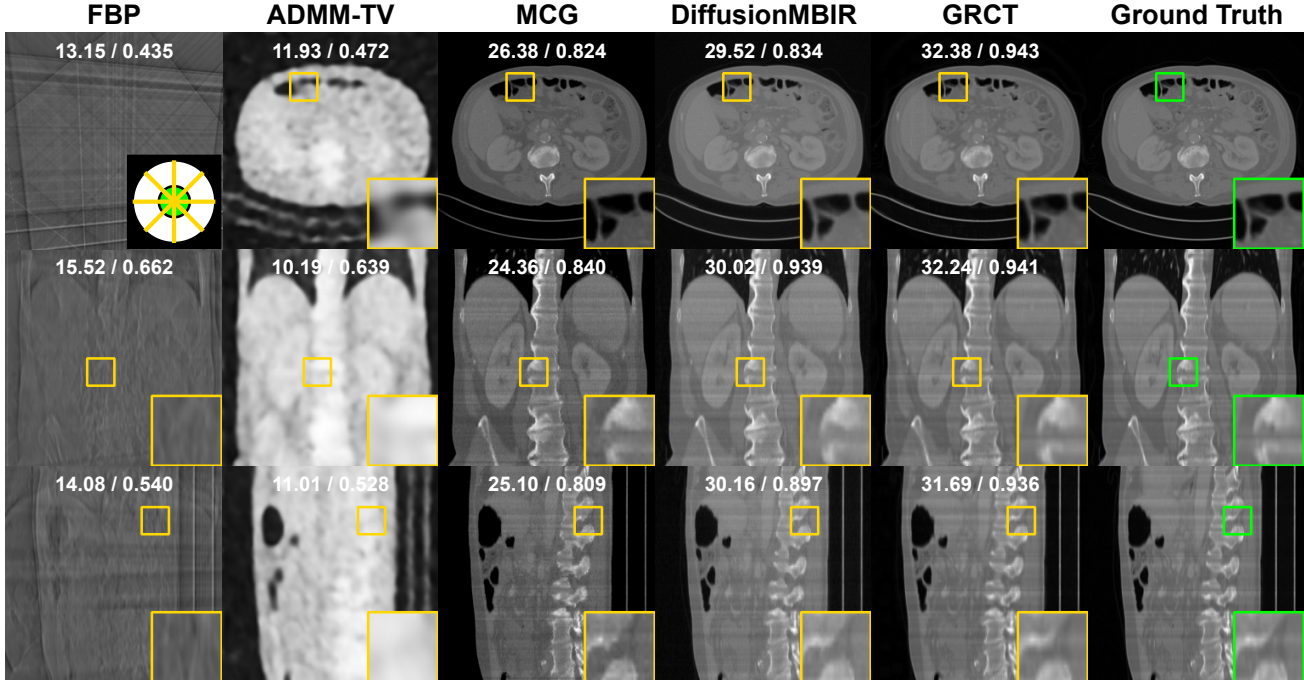| FBP	ADMM-TV	MCG	DiffusionMBIR	GRCT	Ground Truth
13.15 / 0.435	11.93 / 0.472	26.38 / 0.824	29.52 / 0.834	32.38 / 0.943	
15.52 / 0.662	10.19 / 0.639	24.36 / 0.840	30.02 / 0.939	32.24 / 0.941	
14.08 / 0.540	11.01 / 0.528	25.10 / 0.809	30.16 / 0.897	31.69 / 0.936	

Figure 3. Visualization of Different Methods for 4-view SVCT Reconstruction. First Row: Axial View, Second Row: Coronal View, Third Row: Sagittal View. Regions in the golden boxes are zoomed in at the bottom-right corner.

Optimization After reconstructing the 3D volume from the Gaussians, we aim to optimize the parameters of the Gaussians in the projection space. The first step is to project the 3D volume back to the projection space. Our method is not restricted to specific CT configurations such as cone-beam or fan-beam CT, as it supports various geometry projection transformations. We define a general geometry projection transformation $\mathcal{T}$ to project the 3D volume back to the projection space:

$$\hat{P} = \mathcal{T}(V), \tag{12}$$

where $\hat{P} \in \mathbb{R}^{m \times n \times p}$ is the estimated projection.

We optimize the parameters of the Gaussians to minimize the discrepancy between the estimated projection $\hat{P}$ and the reference projection P, guided by L1 loss:

$$\mathcal{L} = ||\hat{P} - P||_1. \tag{13}$$

We also explore other loss functions, such as Total Variation (TV) regularization and Structural Similarity (SSIM) loss in Appendix D. This completes one iteration of the training process. The entire process can be repeated iteratively to refine the reconstruction quality.

5. Experiments

5.1. Experiment Settings

Dataset We conducted experiments using three datasets, including the FIPS dataset [28], AAPM-Mayo LDCT

dataset [26] and FUMPE dataset [23]. The FIPS dataset is a real-world dataset for CBCT reconstruction, and we use three cases (walnut, pine, and seashell) with 721 real projections for each case. The AAPM-Mayo LDCT dataset is widely used for CT reconstruction with 5388 slices of 1mm thickness. The FUMPE dataset consists of 8792 chest CT images, where the thickness is varied from 0.5mm to 5mm. For AAPM-Mayo and FUMPE datasets, we synthesises the projection data using the Operator discretization library (ODL) [1] following common practice in previous research [6, 7, 31].

Implementation Details We implement DGR using Py-Torch and train it on a single NVIDIA RTX 6000 for most experiments, except for the 75/50/25-view SVCT on the FIPS dataset, which is trained on a single NVIDIA RTX 3090 GPU to maintain the same training environment as R^2-Gaussian [35] for fair comparison. We initialize the Gaussians at the beginning of training by the well-established FBP algorithm [2], where the voxels with median gradients are selected as the Gaussian centers, and its covariance matrix is set to the identity matrix, and the intensity is set to the voxel value in the FBP reconstruction. We set the number of Gaussians to 150K at initialization and the size of the local box to $17 \times 17 \times 17$. We use the Adam optimizer with a learning rate of 3e-4 and decay to 3e-5 at the end of training. For 75-view, 50-view, and 25-view cone-beam SVCT, and 2-view, 4-view, and 8-view fan-beam Ultra SVCT, we set the training iteration to 1K. For 180-view, 120-view, 90-

Table 1. Comparisons of 75/50/25-view SVCT on FIPS dataset. Best in **Bold.**

Method	75-view			50-view			25-view		
	PSNR	SSIM	Time	PSNR	SSIM	Time	PSNR	SSIM	Time
FDK [8]	30.03	0.535	-	27.38	0.449	-	23.30	0.335	-
IntraTomo (ICCV 21) [33]	36.79	0.858	2h25m	36.99	0.854	2h19m	35.85	0.835	2h18m
NAF (MICCAI 22) [34]	38.58	0.848	51m28s	36.44	0.818	51m31s	32.92	0.772	51m24s
SAX-NeRF (CVPR 24) [3]	34.93	0.854	13h21m	34.89	0.840	13h23m	33.49	0.793	13h25m
X-Gaussian (ECCV 24) [4]	38.27	0.894	10m21s	37.80	0.881	10m5s	35.12	0.859	9m55s
R^2-Gaussian 10K(NeurIPS 24) [35]	38.10	0.872	3m39s	37.52	0.866	3m37s	35.10	0.840	3m23s
R^2-Gaussian 30K(NeurIPS 24) [35]	39.40	0.875	14m16s	38.24	0.864	13m52s	34.83	0.833	12m56s
Ours (iter=300)	39.91	0.937	**3m36s**	38.66	0.929	**3m24s**	**35.16**	**0.883**	**2m59s**
Ours (iter=1000)	**41.28**	**0.952**	13m14s	**39.27**	**0.940**	11m48s	34.58	0.870	8m54s

Table 2. Comparisons of 180/120/90/60-view SVCT on AAPM-Mayo LDCT dataset. Best in **Bold.**

Method	Extra Data	180-view		120-view		90-view		60-view	
		PSNR	SSIM	PSNR	SSIM	PSNR	SSIM	PSNR	SSIM
FBP [2]	0	31.69	0.882	28.30	0.787	26.20	0.701	23.18	0.595
FBPConvNet (TIP 17) [16]	4839	42.23	0.988	39.45	0.983	37.11	0.976	35.63	0.966
U-Net (TRPMS 18) [21]	4839	38.37	0.985	35.58	0.977	30.09	0.947	28.83	0.937
PLANet (ACM'MM 22) [32]	4176	42.76	0.965	41.67	0.962	40.99	0.957	38.97	0.941
GMSD (TRPMS 23) [11]	4839	41.44	0.988	39.41	0.981	37.25	0.974	34.31	0.958
SWORD (TMI 24) [31]	4839	45.08	0.994	42.49	0.990	41.27	0.986	38.49	0.978
Ours	0	**46.13**	**0.997**	**44.64**	**0.994**	**43.23**	**0.992**	**40.25**	**0.985**

Table 3. AAPM-Mayo LDCT 8-view CT reconstruction.

Method	Data	Axial		Coronal		Sagittal	
		PSNR ↑	SSIM ↑	PSNR ↑	SSIM ↑	PSNR ↑	SSIM ↑
FBP [2]	0	16.31	0.320	16.65	0.320	16.34	0.322
FBPConvNet (TIP 17) [16]	3142	16.57	0.553	19.12	0.774	18.11	0.714
ADMM-TV (TIP 17) [24]	3142	16.79	0.645	18.95	0.772	17.27	0.716
MCG (NeurIPS 22) [6]	3839	28.61	0.873	28.05	0.884	24.45	0.765
Lahiri *et al.* (TCI 23) [20]	3142	21.38	0.711	23.89	0.769	20.81	0.716
DiffusionMBIR (CVPR 23) [7]	3142	33.49	0.942	35.18	**0.967**	32.18	0.910
Ours	0	**35.54**	**0.956**	**37.05**	0.954	**35.65**	**0.956**

Table 4. AAPM-Mayo LDCT 4-view CT reconstruction.

Method	Data	Axial		Coronal		Sagittal	
		PSNR ↑	SSIM ↑	PSNR ↑	SSIM ↑	PSNR ↑	SSIM ↑
FBP [2]	0	13.28	0.206	13.83	0.215	13.33	0.211
FBPConvNet (TIP 17) [16]	3142	16.45	0.529	19.47	0.713	15.48	0.610
ADMM-TV (TIP 17) [24]	3142	13.59	0.618	15.23	0.682	14.60	0.638
MCG (NeurIPS 22) [6]	3839	27.33	0.855	26.52	0.863	23.04	0.745
Lahiri *et al.* (TCI 23) [20]	3142	20.37	0.652	21.41	0.721	18.40	0.665
DiffusionMBIR (CVPR 23) [7]	3142	30.52	0.914	30.09	**0.938**	27.89	0.871
Ours	0	**30.96**	**0.919**	**31.84**	0.930	**31.09**	**0.921**

Table 5. AAPM-Mayo LDCT 2-view CT reconstruction.

Method	Data	Axial		Coronal		Sagittal	
		PSNR ↑	SSIM ↑	PSNR ↑	SSIM ↑	PSNR ↑	SSIM ↑
FBP [2]	0	8.81	0.142	10.30	0.159	8.89	0.147
FBPConvNet (TIP 17) [16]	3142	16.31	0.521	17.05	0.521	11.07	0.483
ADMM-TV (TIP 17) [24]	3142	10.28	0.409	13.77	0.616	11.49	0.553
MCG (NeurIPS 22) [6]	3839	**24.69**	**0.821**	23.52	0.806	20.71	0.685
Lahiri *et al.* (TCI 23) [20]	3142	19.74	0.631	19.92	0.720	17.34	0.650
DiffusionMBIR (CVPR 23) [7]	3142	24.11	0.810	23.15	**0.841**	21.72	0.766
Ours	0	24.06	0.778	**25.46**	0.815	**24.12**	**0.780**

Table 6. AAPM-Mayo LDCT 90° LACT reconstruction.

Method	Data	Axial		Coronal		Sagittal	
		PSNR ↑	SSIM ↑	PSNR ↑	SSIM ↑	PSNR ↑	SSIM ↑
FBP [2]	0	14.91	0.397	17.07	0.411	15.46	0.403
FBPConvNet (TIP 17) [16]	3142	26.76	0.879	25.77	0.874	22.92	0.841
ADMM-TV (TIP 17) [24]	3142	23.19	0.793	22.96	0.758	19.95	0.782
MCG (NeurIPS 22) [6]	3839	26.01	0.838	24.55	0.823	21.59	0.706
Lahiri *et al.* (TCI 23) [20]	3142	28.08	0.931	26.02	0.856	23.24	0.812
DiffusionMBIR (CVPR 23) [7]	3142	34.92	0.956	32.48	0.947	28.82	0.832
Ours	0	**38.22**	**0.970**	**39.32**	**0.969**	**38.35**	**0.970**

view, and 60-view fan-beam SVCT, we did not set the iteration limit, and the training process is stopped when the validation loss converges in the projection space.

5.2. Experimental Results and Analysis

5.2.1. Real-World Cone-Beam SVCT Reconstruction

In Table 1, we compare DGR with cutting-edge scene-reconstruction-based methods on the FIPS dataset, and we follow the same experimental settings as R^2-Gaussian [35] for fair comparison. The baseline methods include both advanced NeRF-based methods IntraTomo [33], NAF [34] and SAX-NeRF [3], and the lastest 3DGS-based methods

X-Gaussian [4] and R^2-Gaussian [35]. The results of X-Gaussian are experimented with official code and the results of other methods are cited from R^2-Gaussian [35].

DGR achieves the best performance in terms of PSNR and SSIM across all view numbers. Specifically, DGR achieves a PSNR of 41.28 dB and an SSIM of 0.952 with 1000 iterations, which outperforms the second-best method R^2-Gaussian 30K by a large margin. Besides, DGR that only trained with 300 iterations also have superior performance compared to most advanced methods while maintaining a low time consumption of about 3 minutes.

Table 7. Comparisons of 180/120/90/60-view SVCT on FUMPE dataset. Best in **Bold.**

Method	Extra Data	180-view		120-view		90-view		60-view	
		PSNR	SSIM	PSNR	SSIM	PSNR	SSIM	PSNR	SSIM
FBP [2]	0	33.74	0.859	30.65	0.803	28.52	0.757	25.59	0.592
MCG (NeurIPS 22) [6]	8341	36.93	0.898	37.05	0.899	37.03	0.899	35.46	0.900
DiffusionMBIR (CVPR 23) [7]	8341	36.78	0.914	36.50	0.907	36.79	0.918	34.86	0.918
SWORD (TMI 24) [31]	8341	41.50	0.967	39.69	0.959	37.77	0.948	31.64	0.910
Ours	0	**41.78**	**0.978**	**40.13**	**0.969**	**38.13**	**0.961**	**36.48**	**0.923**

Table 8. Video-Memory and Time Per Iteration

Method	VRAM (GiB)	Time (s)
Direct	16662.50	/
Fast w/o decomposition	16.87	1.05
Fast w/ decomposition	16.87	0.09

Table 9. Effect of Box Size on 60-view SVCT with 10K iterations

Box-Size	$13 \times 13 \times 13$	$15 \times 15 \times 15$	$17 \times 17 \times 17$	$19 \times 19 \times 19$
Time (h)	1.32	1.85	2.77	4.51
V-Ram (GiB)	10.70	13.29	16.87	21.32
PSNR / SSIM	35.99 / 0.960	38.90 / 0.973	40.25 / 0.985	40.98 / 0.987

5.2.2. Fan-Beam SVCT Reconstruction

In Table 2 and Table 7, we compare DGR with the most advanced DLR methods on the AAPM-Mayo LDCT dataset and FUMPE dataset. 'Extra Data' is the number of slices used for the training of DLR methods, whereas our DGR method does not require any additional data. The baseline methods include traditional CNN-Based methods FBP-ConvNet [16], U-Net [21], PLANet [32], and advanced diffusion-based methods GMSD [11], MCG [6], DiffusionMBIR [7], and SWORD [31]. We follow the setting of 180/120/90/60-view SVCT that used in GMSD and SWORD for fair comparison. DGR achieves the best performance in terms of PSNR and SSIM across all view numbers. Specifically, DGR achieves a PSNR of 46.13 dB and an SSIM of 0.997 with 180 views, which outperforms the second-best method SWORD by a large margin. Moreover, DGR achieves the best performance on the FUMPE dataset, which demonstrates the generalization ability of DGR.

5.2.3. Ultra Sparse-View CT and Limited-Angle CT

In Table 3, Table 4, Table 5, and Table 6, we compare DGR with advanced DLR methods on Ultra Sparse-View CT and Limited-Angle CT reconstruction. The baseline methods include traditional CNN-Based methods FBPConvNet [16], Lahiri *et al.* [20], and advanced diffusion-based methods MCG [6], DiffusionMBIR [7]. We follow the setting of 8/4/2-view SVCT and 90-degree LACT that used in DiffusionMBIR and MCG for fair comparison. DGR achieves the best performance in terms of PSNR and SSIM across all view numbers. Specifically, DGR achieves a PSNR of 35.54 dB and an SSIM of 0.956 with 8 views, which outperforms the two diffusion-based methods DiffusionMBIR and MCG. In 90-degree Limited-Angle CT reconstruction, DGR achieves a PSNR of 38.22 dB and an SSIM of 0.970, which outperforms the DiffusionMBIR by a large margin. In Figure 3, we present visualization of various methods employed for 4-view SVCT reconstruction, with more visualizations provided in Appendix F.

5.3. Ablation Study

Effect of Box Size In Table 9, we evaluate the effect of the box size on 60-view SVCT on AAPM-Mayo LDCT. Each configuration was evaluated over 10,000 iterations to ensure stable assessments of time and video memory usage. We observe that the performance increases as the box size increases, which is because the larger box size provides more context information for the optimization of Gaussians. However, the time consumption and video memory also increase with the box size. We choose $17 \times 17 \times 17$ as the default box size in our experiments, which achieves a good balance between performance and efficiency.

Effect of Fast Volume Reconstruction We compare the video-memory and time consumption of the Direct reconstruction and the Fast Volume Reconstruction in Table 8. We observe that the Fast Volume Reconstruction achieves a significant reduction in time consumption compared to the Direct reconstruction. The decomposition further reduces the time consumption from 1.05s to 0.09s, which enables the efficient reconstruction of DGR.

Effect of View and Angle Selection In Table 1 - Table 7, the results show different performance under multiple views and limited angles. It can be observed that the performance decreases as the number of views decreases in SVCT. This is because the measurements acquired from more views provides more information about the attenuation distribution. The performance of LACT is better than the 8-view SVCT but worse than the 60-view SVCT because the limited angle leads to a loss of information from certain views.

6. Conclusion

In this paper, we rethink the tomography volume reconstruction from the fundamental representation level, and propose an intuitive and efficient method named Discretized Gaussian Reconstruction (DGR). We represent the volume as a set of discretized Gaussians and align their contributions to 3D grid to achieve efficient and accurate CT reconstruction with state-of-the-art performance in terms of both image quality and computational efficiency.

References

[1] Jonas Adler, Holger Kohr, and Ozan Öktem. Operator discretization library (odl). *Zenodo*, 2017. 6

[2] Ronald Newbold Bracewell and ACf Riddle. Inversion of fan-beam scans in radio astronomy. *Astrophysical Journal, vol. 150, p. 427*, 150:427, 1967. 3, 6, 7, 8

[3] Yuanhao Cai, Jiahao Wang, Alan Yuille, Zongwei Zhou, and Angtian Wang. Structure-aware sparse-view x-ray 3d reconstruction. In *Proceedings of the IEEE/CVF Conference on Computer Vision and Pattern Recognition*, pages 11174–11183, 2024. 3, 7

[4] Yuanhao Cai, Yixun Liang, Jiahao Wang, Angtian Wang, Yulun Zhang, Xiaokang Yang, Zongwei Zhou, and Alan Yuille. Radiative gaussian splatting for efficient x-ray novel view synthesis. In *European Conference on Computer Vision*, pages 283–299. Springer, 2025. 1, 3, 7

[5] Hu Chen, Yi Zhang, Mannudeep K Kalra, Feng Lin, Yang Chen, Peixi Liao, Jiliu Zhou, and Ge Wang. Low-dose ct with a residual encoder-decoder convolutional neural network. *IEEE transactions on medical imaging*, 36(12):2524–2535, 2017. 1, 2

[6] Hyungjin Chung, Byeongsu Sim, Dohoon Ryu, and Jong Chul Ye. Improving diffusion models for inverse problems using manifold constraints. *Advances in Neural Information Processing Systems*, 35:25683–25696, 2022. 2, 6, 7, 8

[7] Hyungjin Chung, Dohoon Ryu, Michael T Mccann, Marc L Klasky, and Jong Chul Ye. Solving 3d inverse problems using pre-trained 2d diffusion models. ieee. In *CVF Conference on Computer Vision and Pattern Recognition*, page 6, 2023. 1, 2, 6, 7, 8, 11, 12

[8] Lee A Feldkamp, Lloyd C Davis, and James W Kress. Practical cone-beam algorithm. *Josa a*, 1(6):612–619, 1984. 7

[9] Xueming Fu, Yingtai Li, Fenghe Tang, Jun Li, Mingyue Zhao, Gao-Jun Teng, and S Kevin Zhou. 3dgr-car: Coronary artery reconstruction from ultra-sparse 2d x-ray views with a 3d gaussians representation. In *International Conference on Medical Image Computing and Computer-Assisted Intervention*, pages 14–24. Springer, 2024. 3

[10] Richard Gordon, Robert Bender, and Gabor T Herman. Algebraic reconstruction techniques (art) for three-dimensional electron microscopy and x-ray photography. *Journal of theoretical Biology*, 29(3):471–481, 1970. 2

[11] Bing Guan, Cailian Yang, Liu Zhang, Shanzhou Niu, Minghui Zhang, Yuhao Wang, Weiwen Wu, and Qiegen Liu. Generative modeling in sinogram domain for sparse-view ct reconstruction. *IEEE Transactions on Radiation and Plasma Medical Sciences*, 2023. 7, 8

[12] Yoseob Han and Jong Chul Ye. Framing u-net via deep convolutional framelets: Application to sparse-view ct. *IEEE transactions on medical imaging*, 37(6):1418–1429, 2018. 2

[13] Ji He, Yongbo Wang, and Jianhua Ma. Radon inversion via deep learning. *IEEE transactions on medical imaging*, 39 (6):2076–2087, 2020. 2

[14] Alain Hore and Djemel Ziou. Image quality metrics: Psnr vs. ssim. In *2010 20th international conference on pattern recognition*, pages 2366–2369. IEEE, 2010. 11

[15] Dianlin Hu, Jin Liu, Tianling Lv, Qianlong Zhao, Yikun Zhang, Guotao Quan, Juan Feng, Yang Chen, and Limin Luo. Hybrid-domain neural network processing for sparse-view ct reconstruction. *IEEE Transactions on Radiation and Plasma Medical Sciences*, 5(1):88–98, 2020. 1, 2

[16] Kyong Hwan Jin, Michael T McCann, Emmanuel Froustey, and Michael Unser. Deep convolutional neural network for inverse problems in imaging. *IEEE transactions on image processing*, 26(9):4509–4522, 2017. 1, 2, 7, 8

[17] Eunhee Kang, Junhong Min, and Jong Chul Ye. A deep convolutional neural network using directional wavelets for low-dose x-ray ct reconstruction. *Medical physics*, 44(10):e360–e375, 2017. 2

[18] Bernhard Kerbl, Georgios Kopanas, Thomas Leimkühler, and George Drettakis. 3d gaussian splatting for real-time radiance field rendering. *ACM Transactions on Graphics*, 42 (4):1–14, 2023. 2, 3

[19] Lennart Koetzier, Domenico Mastrodicasa, Timothy Szczykutowicz, Niels Werf, Adam Wang, Veit Sandfort, Aart van der Molen, Dominik Fleischmann, and Martin Willemink. Deep learning image reconstruction for ct: Technical principles and clinical prospects. *Radiology*, 306, 2023. 1

[20] Anish Lahiri, Gabriel Maliakal, Marc L Klasky, Jeffrey A Fessler, and Saiprasad Ravishankar. Sparse-view cone beam ct reconstruction using data-consistent supervised and adversarial learning from scarce training data. *IEEE Transactions on Computational Imaging*, 9:13–28, 2023. 7, 8

[21] Hoyeon Lee, Jongha Lee, Hyeongseok Kim, Byungchul Cho, and Seungryong Cho. Deep-neural-network-based sinogram synthesis for sparse-view ct image reconstruction. *IEEE Transactions on Radiation and Plasma Medical Sciences*, 3(2):109–119, 2018. 7, 8

[22] Yiqun Lin, Hualiang Wang, Jixiang Chen, and Xiaomeng Li. Learning 3d gaussians for extremely sparse-view cone-beam ct reconstruction, 2024. 3

[23] Mojtaba Masoudi, Hamid-Reza Pourreza, Mahdi Saadatmand-Tarzjan, Noushin Eftekhari, Fateme Shafiee Zargar, and Masoud Pezeshki Rad. A new dataset of computed-tomography angiography images for computer-aided detection of pulmonary embolism. *Scientific data*, 5 (1):1–9, 2018. 6, 11

[24] Michael T McCann, Masih Nilchian, Marco Stampanoni, and Michael Unser. Fast 3d reconstruction method for differential phase contrast x-ray ct. *Optics express*, 24(13):14564–14581, 2016. 4, 7

[25] Ben Mildenhall, Pratul P Srinivasan, Matthew Tancik, Jonathan T Barron, Ravi Ramamoorthi, and Ren Ng. Nerf: Representing scenes as neural radiance fields for view synthesis. *Communications of the ACM*, 65(1):99–106, 2021. 2, 3

[26] Taylor R Moen, Baiyu Chen, David R Holmes III, Xinhui Duan, Zhicong Yu, Lifeng Yu, Shuai Leng, Joel G Fletcher, and Cynthia H McCollough. Low-dose ct image and projection dataset. *Medical physics*, 48(2):902–911, 2021. 6, 11

[27] Olaf Ronneberger, Philipp Fischer, and Thomas Brox. U-net: Convolutional networks for biomedical image segmen-

tation. In *Medical image computing and computer-assisted intervention–MICCAI 2015: 18th international conference, Munich, Germany, October 5-9, 2015, proceedings, part III 18*, pages 234–241. Springer, 2015. 2, 3

[28] The Finnish Inverse Problems Society. X-ray tomographic datasets, 2024. 6, 11, 12

[29] Timothy P Szczykutowicz, Giuseppe V Toia, Amar Dhanant-wari, and Brian Nett. A review of deep learning ct reconstruction: concepts, limitations, and promise in clinical practice. *Current Radiology Reports*, 10(9):101–115, 2022. 1

[30] Zhou Wang, Alan C Bovik, Hamid R Sheikh, and Eero P Simoncelli. Image quality assessment: from error visibility to structural similarity. *IEEE transactions on image processing*, 13(4):600–612, 2004. 11

[31] Kai Xu, Shiyu Lu, Bin Huang, Weiwen Wu, and Qiegen Liu. Stage-by-stage wavelet optimization refinement diffusion model for sparse-view ct reconstruction. *IEEE Transactions on Medical Imaging*, 2024. 1, 2, 6, 7, 8, 11

[32] Liutao Yang, Rongjun Ge, Shichang Feng, and Daoqiang Zhang. Learning projection views for sparse-view ct reconstruction. In *Proceedings of the 30th ACM International Conference on Multimedia*, pages 2645–2653, 2022. 7, 8

[33] Guangming Zang, Ramzi Idoughi, Rui Li, Peter Wonka, and Wolfgang Heidrich. Intratomo: self-supervised learning-based tomography via sinogram synthesis and prediction. In *Proceedings of the IEEE/CVF International Conference on Computer Vision*, pages 1960–1970, 2021. 3, 7

[34] Ruyi Zha, Yanhao Zhang, and Hongdong Li. Naf: neural attenuation fields for sparse-view cbct reconstruction. In *International Conference on Medical Image Computing and Computer-Assisted Intervention*, pages 442–452. Springer, 2022. 3, 7

[35] Ruyi Zha, Tao Jun Lin, Yuanhao Cai, Jiwen Cao, Yanhao Zhang, and Hongdong Li. R^2-gaussian: Rectifying radiative gaussian splatting for tomographic reconstruction. In *Advances in Neural Information Processing Systems (NeurIPS)*, 2024. 1, 2, 3, 6, 7, 11

[36] Bo Zhu, Jeremiah Z Liu, Stephen F Cauley, Bruce R Rosen, and Matthew S Rosen. Image reconstruction by domain-transform manifold learning. *Nature*, 555(7697):487–492, 2018. 2

Appendix

A. Overview

Thank you for reading the Appendix of our DGR. The appendix is organized as follows: First, we provide a detailed explanation of the experimental setup in Section B. Next, we describe the evaluation metrics used in our study in Section C. Following that, we discuss the use of different loss functions in Section D. In Section E, we elaborate on the details of Fast Volume Reconstruction and analyze its computational complexity. Finally, Section F presents additional visualizations of DGR reconstruction.

B. Experiment Details

B.1. Code and Reproducibility

We have included our code in the attachment and organized it carefully to ensure better readability. The experiments are divided into three groups, each with its corresponding code: (1) Cone-Beam Sparse-View CT, (2) Fan-Beam Sparse-View CT, and (3) Fan-Beam Limited Angle CT. To reproduce our results, we recommend starting with the **Readme.md** file, which provides detailed instructions and guidance.

B.2. Organization of Experiments

To address the varying experimental settings used in related research (e.g., projection numbers, evaluation metrics), we divided our experiments into three groups:
Cone-Beam CT (CBCT): Experiments with 75, 50, and 25 views conducted on the FIPS dataset [28], following the latest research R^2-Gaussian [35] that published at NeurIPS 2024.
Fan-Beam CT (FBCT): Experiments with 180, 120, 90, and 60 views performed on the AAPM-Mayo LDCT dataset [26] and the FUMPE dataset [23] following the recent advanced DLR method SWORD [31] that published at TMI 2024.
Ultra Sparse-View CT (SVCT) and Limited-Angle CT (LACT): Experiments with 8, 4, and 2 views, as well as 90-degree limited-angle CT, conducted on the AAPM-Mayo LDCT dataset [26], following the methodology of DiffusionMBIR [7].

C. Evaluation Metrics

In this section, we describe the evaluation metrics used in the paper.

C.1. Peak Signal-to-Noise Ratio (PSNR)

The PSNR [14] is a widely used metric to evaluate the quality of the reconstructed images. It is defined as:

$$\text{PSNR}(x, y) = 10 \cdot \log_{10}\left(\frac{\text{MAX}^2}{\text{MSE}(x, y)}\right), \quad (14)$$

Table 10. Usage of Different Loss Functions

Cone Beam SVCT (50 view, 300 iter)				
L1 Loss	SSIM Loss	TV Loss	PSNR	SSIM
✓			38.66	0.929
✓	✓		38.94	0.933
✓	✓	✓	**39.65**	**0.939**

Table 11. Usage of Different Loss Functions

Fan Beam SVCT (60 view, 300 iter)				
L1 Loss	SSIM Loss	TV Loss	PSNR	SSIM
✓			38.82	0.931
✓	✓		38.88	0.933
✓	✓	✓	**39.15**	**0.936**

Table 12. Usage of Different Loss Functions

Fan Beam LACT (90-degree, 300 iter)				
L1 Loss	SSIM Loss	TV Loss	PSNR	SSIM
✓			37.69	0.932
✓	✓		37.81	0.934
✓	✓	✓	**38.02**	**0.936**

where MAX is the maximum possible pixel value of the image and $\text{MSE}(x, y)$ is the mean squared error between the original and reconstructed images.

C.2. Structural Similarity Index (SSIM)

The SSIM [30] is a metric that measures the similarity between two images. It is defined as:

$$\text{SSIM}(x, y) = \frac{(2\mu_x\mu_y + C_1)(2\sigma_{xy} + C_2)}{(\mu_x^2 + \mu_y^2 + C_1)(\sigma_x^2 + \sigma_y^2 + C_2)}, \quad (15)$$

where μ_x and μ_y are the mean values of the images x and y, σ_x^2 and σ_y^2 are the variances of the images, σ_{xy} is the covariance of the images, and C_1 and C_2 are constants to stabilize the division with weak denominator.

C.3. Evaluation Details

In the 180/120/90/60-view Fan-Beam SVCT experiments, we evaluate the performance of the reconstruction methods across the entire 3D volume following the practice in SWORD [31]. In this paradigm, the x and y in the PSNR and SSIM metrics are the reconstructed 3D volume and the ground truth 3D volume, respectively.

In the 75/50/25-view Cone-Beam SVCT experiments, we assess performance across the test set of the FIPS dataset [28], maintaining the original dataset split to ensure consistency.

In the 8/4/2-view Fan-Beam SVCT and 90-degree LACT experiments, we evaluate the performance across axial,
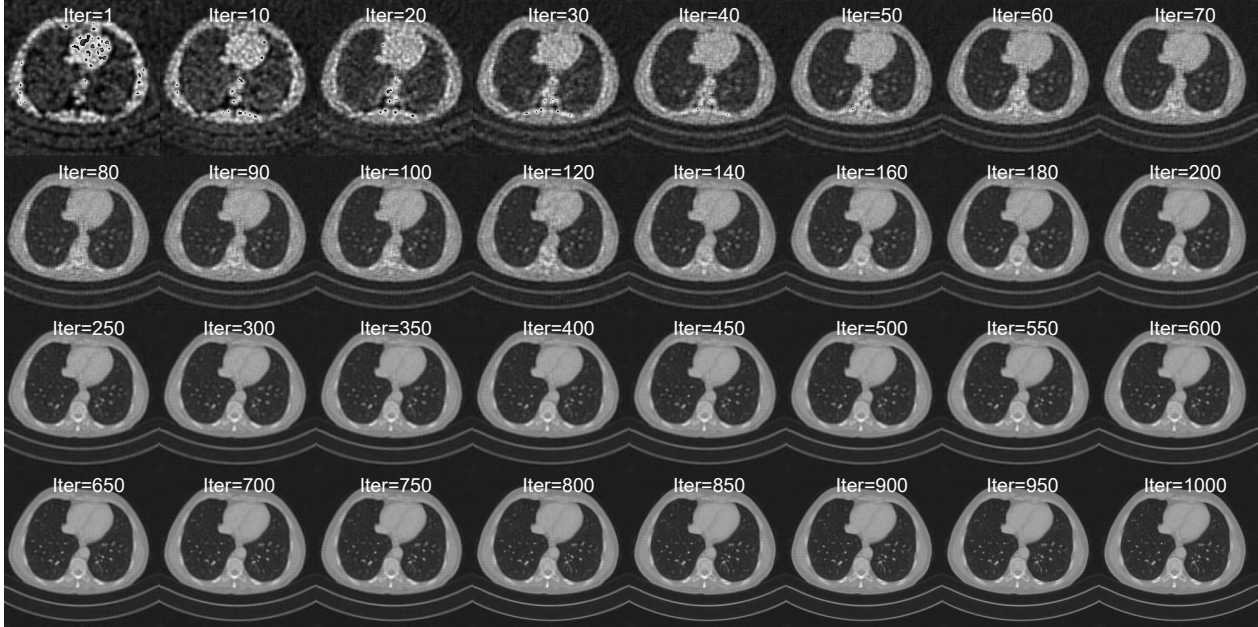
Figure 4. This figure illustrates the reconstruction process by iterations of Fan-Beam 60-view SVCT. We initialize the position of Gaussians with Filtered Back Projection as described in the experiment settings.

coronal, and sagittal slices following DiffusionMBIR [7]. In this paradigm, the x and y in the PSNR and SSIM metrics are the reconstructed 2D slice and the ground truth 2D slice, respectively, and the mean PSNR and SSIM values are computed across all slices.

D. Discussion of Different Losses

In the main text, we adopt only the L1 loss for reconstruction. However, combining different loss functions can further enhance reconstruction quality. Specifically, the SSIM loss is computed in the projection domain to preserve structural information, while the TV loss is computed in the volume domain to promote sparsity in the reconstructed volume.

$$\mathcal{L}_{total} = \lambda_1 \mathcal{L}_{L1} + \lambda_2 \mathcal{L}_{SSIM} \quad (16)$$

where $\lambda_1 = 0.8$ and $\lambda_2 = 0.2$ are the weights of the L1 loss and SSIM loss, respectively.

A combined use of L1 loss, SSIM loss, and TV loss is as follows:

$$\mathcal{L}_{total} = \lambda_1 \mathcal{L}_{L1} + \lambda_2 \mathcal{L}_{SSIM} + \lambda_3 \mathcal{L}_{TV} \quad (17)$$

where $\lambda_1 = 0.6$, $\lambda_2 = 0.2$, and $\lambda_3 = 1$ are the weights of the L1 loss, SSIM loss, and TV loss, respectively.

We present the results for these loss combinations in Table 10, Table 11, and Table 12, corresponding to Cone-Beam SVCT, Fan-Beam SVCT, and Fan-Beam LACT experiments on the real-world FIPS dataset [28]. The results demonstrate that the combined use of L1 loss, SSIM loss, and TV loss achieves the best performance in terms of PSNR and SSIM metrics.

E. Fast Volume Reconstruction

E.1. Highly Parallelized Implementation

We show the detailed implementation of our Fast Volume Reconstruction In Algorithm 1. The algorithm takes the mean μ, covariance C, and intensity I of the Gaussians as input and reconstructs the 3D volume in a fast and efficient manner. Notably, this process is implemented in a highly parallelized manner to accelerate the computation without sacrificing the reconstruction quality. A more engineering-focused implementation is available in the codebase. Please refer to the `fast_volume_reconstruction` function in the code for further details.

E.2. Analysis of Complexity

Method	VRAM (GiB)	Time (s)
Direct	16662.50	/
Fast w/o decomposition	16.87	1.05
Fast w/ decomposition	16.87	0.09

As mentioned in the ablation study, the proposed fast volume reconstruction saves both time and space consumption. The complexity difference lies in the computation of the Mahalanobis distance D^2.
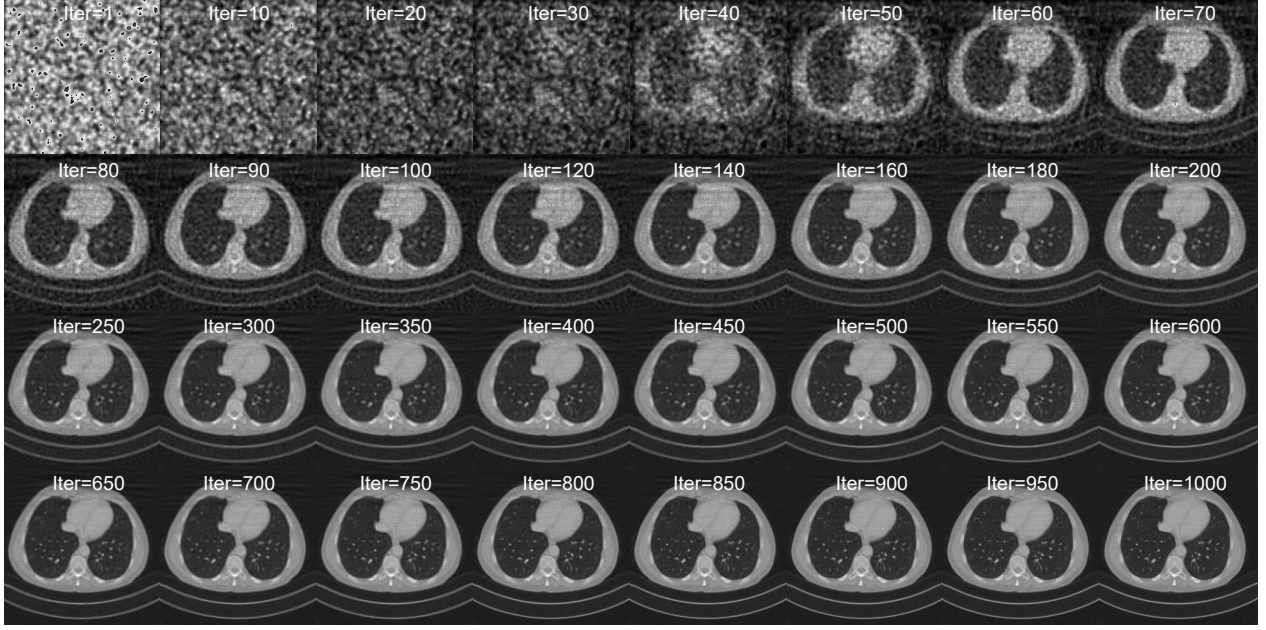
Figure 5. This figure illustrates the reconstruction process by iterations of Fan-Beam 90-degree LACT. We initialize the position of Gaussians randomly for visualization comparison.

Direct Reconstruction We have $D^2 = (P - \mu)^\top \Sigma^{-1} (P - \mu)$. Here, $P \in \mathcal{R}^{w,h,c,d}$ is the position of the voxel where $(d = 3)$ indicates the dimension, $\mu \in \mathcal{R}^{n,d}$ is the set containing n gaussians, and $\Sigma \in \mathcal{R}^{n,d,d}$ is the covariance matrix of the Gaussians. The complexity of the direct reconstruction is $O(n \cdot w \cdot h \cdot c \cdot d^2)$. Obviously, the direct reconstruction is not feasible for large amounts of Gaussians due to the high memory consumption.

Fast Volume Reconstruction without Decomposition We have $D^2 = \sum_d B''_{n,w_0,h_0,c_0,d} C^{-1}_{n,d,d} B''_{n,w_0,h_0,c_0,d.}$, where w_0, h_0, and c_0 are the size of local region. The complexity of the fast volume reconstruction without decomposition is $O(n \cdot w_0 \cdot h_0 \cdot c_0 \cdot d^2)$. Compared to the direct reconstruction, the local region size $w_0 \cdot h_0 \cdot c_0$ is much smaller than the volume size $w \cdot h \cdot c$, which significantly reduces the memory consumption.

Fast Volume Reconstruction with Decomposition The decomposed form of Fast Volume Reconstruction yields:

$$D^2 = \sum_d \left(B'_{w_0,h_0,c_0,d} - \Delta\mu_{n,1,1,d} \right) C^{-1}_{n,d,d} \left(B'_{w_0,h_0,c_0,d} - \Delta\mu_{n,1,1,d} \right)$$

The space complexity is the same as the fast volume reconstruction without decomposition, the time complexity is significantly reduced to $O(w_0 \cdot h_0 \cdot c_0 \cdot d)$ benefiting from the decomposition of the large matrix multiplication.

F. Visualization

We provide additional visualizations to demonstrate the effectiveness of our DGR in Incomplete CT Reconstruction.

F.1. Reconstruction Process Visualization

Figures 4 and 5 showcase the reconstruction process over iterations, with the iteration number indicated at the top of each image. For comparison, the Gaussians for SVCT are initialized as described in the main text, while the Gaussians for LACT are initialized randomly. As the iterations progress, the reconstructions steadily improve, demonstrating the effectiveness of our approach.

F.2. Reconstruct Bone Structure

In Figure 6, we visualize the reconstructed 3D bone structures under the 8-view SVCT setting. The bone structures are extracted from the reconstructed 3D volumes using an intensity threshold of 140 (on a 0–255 scale). The results show that our method generates more accurate and detailed bone structures compared to the advanced diffusion-based method DiffusionMBIR.

F.3. Gaussians Visualization

Figure 7 illustrates the Gaussians generated by our DGR, visualized from multiple perspectives to highlight their 3D spatial distribution. Despite the absence of pretraining on full projections or CT images, the Gaussians effectively capture underlying structures guided solely by projection data, which demonstrates the adaptability of our approach.

Figure 6. 3D Visualization of the reconstructed 3D bones of different methods under 8-view SVCT. Our DGR (middle) generates more accurate and detailed bone structures compared to the advanced method DiffusionMBIR (left), with the ground truth (right) as reference. Isometric views are shown for better visualization.
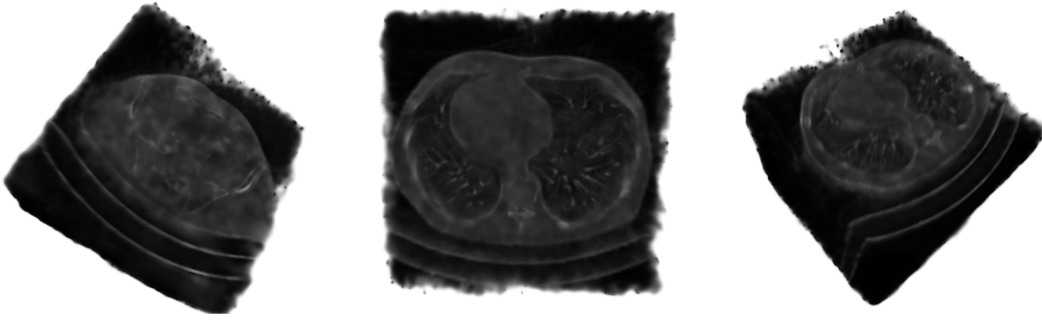

Figure 7. The 3D visualization of the Gaussians generated by our DGR. The Gaussians are visualized from different perspectives to show the distribution of the Gaussians in the 3D space.

Algorithm 1 Fast Volume Reconstruction

Require: $\mu \in \mathbb{R}^{n \times d}$: mean of Gaussians ($d = 3$ for 3D space)
Require: $C \in \mathbb{R}^{n \times d \times d}$: covariance of Gaussians
Require: $I \in \mathbb{R}^{n \times 1}$: intensity of Gaussians

$V \leftarrow \mathbf{O}_{w,h,c}$ ▷ Initialize target volume with zeros

$B'_{w_0,h_0,c_0,d} \leftarrow \texttt{meshgrid}(\{-\frac{w_0-1}{2}, \ldots, \frac{w_0-1}{2}\}, \{-\frac{h_0-1}{2}, \ldots, \frac{h_0-1}{2}\}, \{-\frac{c_0-1}{2}, \ldots, \frac{c_0-1}{2}\})$ ▷ Initialize the shift of local regions

$\Delta\mu \leftarrow \mu - \lfloor\mu\rfloor$ ▷ Align μ to discrete voxel grid

$B'^T C^{-1} B'_{n,w_0,h_0,c_0} \leftarrow \sum_d B'_{w_0,h_0,c_0,d} C^{-1}_{n,d,d} B'_{w_0,h_0,c_0,d}$ ▷ Decompose large matrix multiplication

$B'^T C^{-1} \Delta\mu_{n,w_0,h_0,c_0} \leftarrow \sum_d B'_{w_0,h_0,c_0,d} C^{-1}_{n,d,d} \Delta\mu_{n,1,1,d}$

$\Delta\mu^T C^{-1} B'_{n,w_0,h_0,c_0} \leftarrow \sum_d \Delta\mu_{n,1,1,d} C^{-1}_{n,d,d} B'_{w_0,h_0,c_0,d}$

$\Delta\mu^T C^{-1} \Delta\mu_{n,1,1,1} \leftarrow \sum_d \Delta\mu_{n,1,1,d} C^{-1}_{n,d,d} \Delta\mu_{n,1,1,d}$

$\Gamma \leftarrow e^{-\frac{1}{2}(B'^T C^{-1} B' + B'^T C^{-1} \Delta\mu + \Delta\mu^T C^{-1} B' + \Delta\mu^T C^{-1} \Delta\mu)} \cdot I$ ▷ Compute the Gaussian contributions

$P_{n,w_0,h_0,c_0,d} \leftarrow \lfloor\mu\rfloor_{n,1,1,1,d} + B'$ ▷ Compute the voxel positions that the Gaussians will impact

$Valid_{n,w_0,h_0,c_0} \leftarrow (P_{n,w_0,h_0,c_0,0} \geq 0) \wedge (P_{n,w_0,h_0,c_0,0} < w) \wedge (P_{n,w_0,h_0,c_0,1} \geq 0) \wedge (P_{n,w_0,h_0,c_0,1} < h) \wedge (P_{n,w_0,h_0,c_0,2} \geq 0) \wedge (P_{n,w_0,h_0,c_0,2} < c)$ ▷ Get valid indices that are within the volume

$V \leftarrow \texttt{scatter\_add}(V, P[Valid], \Gamma[Valid])$ ▷ Accumulate the contributions at the valid indices parallelly

return V ▷ Reconstructed CT volume